scientific reports

Check for updates

OPEN

Enhanced efficacy of combined VEGFR peptide–drug conjugate and anti-PD-1 antibody in treating hepatocellular carcinoma

Jiacheng Liu[1,2,9], Yaowei Bai[1,2,9], Xiaoming Liu[1,2,9], Binqian Zhou[3], Peng Sun[4], Yingliang Wang[1,2], Shuguang Ju[1,2], Chen Zhou[1,2], Chaoyang Wang[1,2], Wei Yao[1,2], Huihui Yang[5], Xin Jiang[6], Lian Yang[1,2✉], Dongyuan Wang[7,8✉] & Chuansheng Zheng[1,2✉]

This study aimed to design a VEGFR-targeting peptide–drug conjugate with the ability to decrease tumor burden and suppress tumor angiogenesis, and to further evaluate the therapeutic effect of anti-PD-1 antibody in HCC therapy. A VEGFR-targeting peptide VEGF$_{125-136}$ (QR) was conjugated with a lytic peptide (KLU) to form a peptide–drug conjugate QR-KLU. And the efficacy of QR-KLU in combination with anti-PD-1 antibody for HCC therapy in vivo and in vitro were evaluated. QR-KLU inhibited the proliferation and migration of mouse HCC cell line (Hepa1–6) cells under normoxic and hypoxic conditions in a dose-dependent manner. In the subcutaneous Hepa1–6 tumor model, QR-KLU combined with the anti-PD-1 antibody substantially inhibited tumor growth, promoted tumor necrosis, and prolonged the survival time of tumor-bearing mice. QR-KLU substantially inhibited hypoxia-induced expression of VEGF, promoted tumor vascular normalization, and increased cluster of differentiation 8$^+$ (CD8$^+$) T cell infiltration in the tumor. In addition, QR-KLU and anti-PD-1 antibody demonstrated a strong synergistic effect in promoting the activation of intratumoral CD8$^+$ T cells, reducing the expression of immune-inhibitory factors, and increasing the expression of immune-stimulatory factors. This study proposed a novel approach for enhancing the efficacy of anti-PD-1 antibody using a VEGFR-targeting peptide–drug conjugate in HCC therapy.

Keywords Angiogenesis, anti-PD-1 antibody, Peptide–drug conjugate, Tumor burden, Tumor vascular normalization

Primary liver cancer is the sixth most common type of cancer and the third leading cause of cancer-related deaths worldwide, and hepatocellular carcinoma (HCC) is the most common type among these[1–3]. The efficacy of various treatment options available is generally limited. Tumor microenvironment factors, such as hypoxia and angiogenesis, facilitate tumor growth and invasion[4–6].

Vascular endothelial growth factor (VEGF) is the most crucial angiogenic factor, and VEGF receptor (VEGFR)-targeted agents, such as sorafenib, are commonly used for advanced HCC treatment[7,8]. However, sorafenib only provides a mean survival benefit of approximately 3 months in patients with HCC and is associated with substantial adverse effects[9]. Immunotherapy, predominantly the use of immune checkpoint inhibitors (ICIs) such as anti-programmed cell death receptor-1 (PD-1) antibodies, has been encouraging due to its ability to activate CD8$^+$ T cells, promote tumor infiltration, and block the PD-1/programmed death-ligand 1 (PD-L1) binding, thereby exerting anti-tumor effects[10,11]. VEGF in the tumor microenvironment and circulation has been demonstrated to have immunosuppressive effects, such as inhibiting the activation of transcription

factor nuclear factor-kappa B and dendritic cell maturation by binding to VEGFR1[12,13]. Additionally, VEGF promotes the recruitment of regulatory T cells and myeloid-derived suppressor cells (MDSCs), transitioning from a supportive to an inhibitory tumor immune microenvironment[14].

In recent studies, anticancer peptides (ACPs) have exhibited promising results for HCC treatment[15–18]. Peptides are considered more desirable than antibodies and small molecules because of their high specificity, low systemic toxicity, and superior tumor penetration[19,20]. Furthermore, ACPs are unlikely to exhibit cross-resistance to chemotherapeutic agents[21].

In light of these challenges in HCC treatment, our study embarked on designing a novel VEGFR-targeting peptide-drug conjugate (PDC). This PDC combines a VEGFR-targeting peptide, specifically VEGF$_{125-136}$ (QKRKRKKSRYKS, QR)[22–24], known for its affinity to VEGFR but with limited potency in reducing tumor burden, with a lytic peptide (KLUKLUKKLUKLUK, KLU)[25]. The conjugation of QR with KLU, resulting in a peptide-conjugated drug called QR-KLU, aims to enhance the therapeutic potency. We anticipated that this innovative conjugate would not only activate immune responses but also synergistically enhance anti-tumor efficacy when combined with anti-PD-1 antibody, offering new avenues for HCC treatment. The synthesis method, including high-performance liquid chromatography (HPLC) and mass spectrometry (MS) data of QR, KLU, and QR-KLU, is elaborated in our prior work[26].

Therefore, the primary aim of this study is to evaluate the therapeutic efficacy of QR-KLU in the context of HCC therapy, particularly in conjunction with anti-PD-1 antibodies, to explore its potential as a more effective treatment strategy against this challenging cancer (Fig. 1).

Methods

Hemolysis assay

Blood was taken from healthy rabbits and about 10 times the amount of 0.9% sodium chloride solution was added and centrifuged to obtain the erythrocyte suspension. The red blood cells were co-incubated with the drugs in a constant-temperature water bath for 1 h at 37 °C to evaluate the hemolytic effect of QR, KLU, and QR-KLU at various concentrations. After centrifugation at 3000 rpm for 10 min, the supernatant was collected and the absorbance was measured at 576 nm using an ultraviolet-visible spectrophotometer (Shimazu, Kyoto, Japan). We used 0.1% Triton X-100 (Abcam, Cambridge, UK) and saline as positive and negative controls, respectively. The percentage of hemolysis was calculated using the following formula: Hemolysis (%) = (OD576 sample − OD576 negative control)/(OD576 positive control − OD576 negative control) × 100%.

Cell culture

The mouse HCC cell line Hepa1–6 cells (ATCC, MD, USA) were cultured in Dulbecco's modified Eagle's medium with 10% (v/v) fetal bovine serum (FBS) and penicillin/streptomycin (0.1 mg/mL) in an incubator maintained at 5% CO_2 and a constant temperature of 37 °C. All reagents were purchased from Gibco (CA, USA).
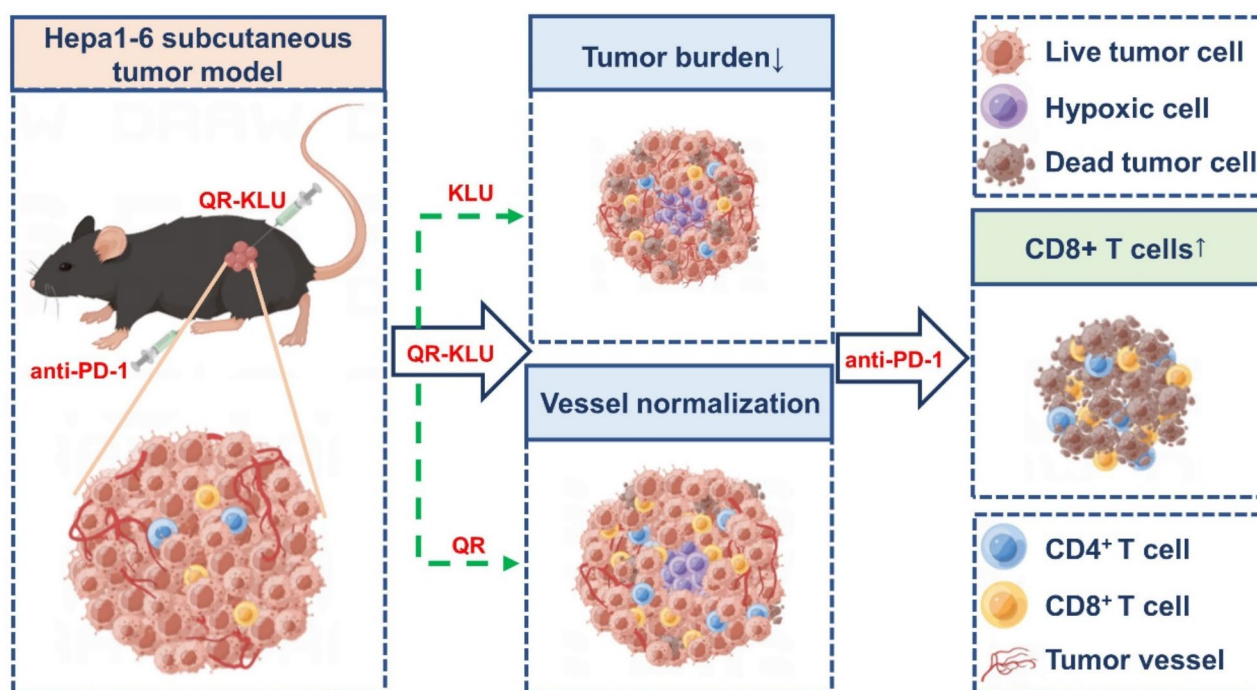

Fig. 1. Schematic diagram of the mechanism of QR-KLU combined with anti-PD-1 antibody for treating subcutaneous Hepa1–6 liver tumors in mice (drawn using Figdraw). *PD-1* programmed cell death receptor-1, *QR-KLU* peptide (QR)–drug (KLU) conjugate.

We mimicked hypoxia condition by adding 100 μM cobalt dichloride ($CoCl_2$; Sigma, St. Louis, MO, USA) to the complete medium with the culture condition described as preceding text. The cell line was authenticated by the manufacturer of the cells using Short Tandem Repeat profiling to ensure that the cells were not misidentified and cross-contaminated.

Cell viability assay

The cell viability for various cell lines was measured using the Cell Counting Kit-8 (CCK8) assays (Abcam, Cambridge, UK). The Hepa1–6 cells were separately seeded in 96-well plates with 200 μL (5×10^4 cells/mL) of the medium per well. Various concentrations of doxorubicin (DOX), QR, KLU, and QR-KLU were then added, and the cells were incubated for 24 h. The medium was subsequently discarded, and 100 μL of fresh medium was added to each well. Following this, 10 μL of CCK8 solution was added, and the cells were incubated for 1 h at 37 °C in a 5% CO_2 atmosphere. The absorbance was measured using a microplate reader (Bio-Rad, CA, USA) at a wavelength of 450 nm.

Colony formation assay

The colony formation assay was used to assess cell proliferation; the assay was conducted as described previously[27]. The Hepa1–6 cells were trypsinized and seeded onto 6-well plates with 500 cells per well under normoxic and hypoxic conditions. After 14 days, the cells were fixed and stained with 0.1% crystal violet. A collection of cells was considered a colony when more than 50 cells were present.

Wound-healing assay

The wound-healing assay was conducted according to the protocols reported by Liang et al.[28]. Briefly, 10^5 Hepa1–6 cells were plated into 12-well plates. After the formation of an adherent confluent monolayer, a wound was created by scratching the monolayer cells with a pipette tip. Then, the cells were treated with KLU and QR-KLU for 24 h under normoxic and hypoxic conditions. The images were collected with a Leica DFC480 camera (Leica, Wetzlar, Germany) on a phase-contrast microscope equipped with a 10 × objective at room temperature. The free area of the wound was measured using Image-Pro Plus V6.0 (Media Cybernetics, Maryland, USA).

Cell apoptosis assay

The cell apoptosis assay was performed using a fluorescein isothiocyanate (FITC) Annexin V Apoptosis Detection Kit I (BD Pharmingen, CA, USA) following the manufacturer's protocol. Briefly, the Hepa1–6 cells were seeded in a 12-well plate and allowed to grow for 24 h. Then, the cells were treated with QR, KLU, and QR-KLU in a medium with 5% FBS for 24 h under normoxic and hypoxic conditions. The cells were collected using 0.25% trypsin- ethylenediaminetetraacetic acid, washed with phosphate-buffered saline (PBS), and suspended in 1× binding buffer for flow cytometry analysis. The apoptotic cells were determined by staining with FITC-labeled Annexin V and propidium iodide (PI). The data were analyzed using the FlowJo software (Bd Biosciences, CA, USA).

Cell cycle analysis

A Cell Cycle Analysis Kit (Beyotime, China) was used for cell cycle assays. Hepa1–6 cells were seeded in a 12-well plate using a growth medium with 10% FBS and allowed to grow for 24 h. Subsequently, the cells were treated with QR, KLU, and QR-KLU in a medium containing 5% FBS for 24 h under normoxic and hypoxic conditions. Following the treatment, the cells were washed with PBS and harvested using 0.25% trypsin-EDTA. After centrifugation, the cells were fixed in 70% cold ethyl alcohol overnight. After another round of washing with PBS, the cells were resuspended and stained with PI in the dark for 30 min following the manufacturer's instructions. The stained samples were then analyzed using a flow cytometer, and the percentage of cells in G0/G1, S, and G2/M phases were determined using the FlowJo software (Bd Biosciences, CA, USA).

Western blot analysis

For Western blot analysis, Hepa1–6 cells were seeded in 12-well plates and incubated for 24 h. Subsequently, the cells were treated with PBS and QR-KLU in a medium containing 5% FBS for 24 h under normoxic and hypoxic conditions. Following the treatment, they were washed with PBS and harvested using radioimmunoprecipitation assay lysis buffer. Protien concentrations were determined using a spectrophotometer (NanoDrop ND-2000, Thermo Fisher Scientific, MA, USA). Equal amounts of protein were then loaded onto sodium dodecyl sulfate–polyacrylamide gels and resolved by electrophoresis. The protein bands were transferred to 0.22-μm polyvinylidene difluoride membranes and incubated overnight at 4 °C with appropriate primary antibodies. The antibodies used included anti-HIF-1α (Abcam, Cambridge, UK) and anti-VEGF (Abcam, Cambridge, UK) at a 1:1000 dilution. Membranes were then washed with a buffer (1× Tris-buffered saline and 0.05% Tween 20). Secondary antibodies were used for incubation at room temperature for 1 h. The proteins were visualized using chemiluminescent substrates. The Western blot quantification was performed using Image-Pro Plus 6.0 software.

Animal and subcutaneous Hepa1–6 tumor model

The male C57BL/6 mice (age, 6–8 weeks; weight, 20–23 g) were purchased from the experimental animal center of Tongji Medical College, Huazhong University of Science and Technology. They were kept in an environment with a cycle of 12 h of light:12 h of dark and a temperature of 20℃–30℃ with a sufficient supply of food and water. All animal experimental operations followed the Guide for the Care and Use of Laboratory Animals published by the National Institutes of Health. The study protocol conformed to the guidelines of the ARRIVE and was approved by the Ethics Committee of Tongji Medical College, Huazhong University of Science and Technology.

Once the Hepa1–6 cells were cultured to the logarithmic growth phase, 1×10^7 cells were injected into the bilateral symmetrical back of the mice. Then, the longest (a) and shortest (b) diameters of the subcutaneous tumors were dynamically monitored using an electronic caliper every other day, and the tumor volume was calculated $(V = a \times b^2/2)$[29]. At the same time, the mice were weighed, and their weights were recorded. These tumor-bearing mice were administered with different drugs when the tumor volume was approximately 100–120 mm^3.

Groups and treatments
The tumor-bearing mice were randomly divided into 6 groups (each with 12 animals): PBS, KLU, QR-KLU, anti-PD-1, KLU + anti-PD-1, and QR-KLU + anti-PD-1. The first day of intervention was defined as day 0. On days 0, 3, 6, and 9, 20 μL of PBS, KLU, or QR-KLU was injected into the tumor. On days 1, 4, 7, and 11, 100 μL of anti-PD-1 antibody (TopAlliance Biosciences, China) was intraperitoneally injected. The doses of KLU, anti-PD-1, and QR-KLU were all 10 mg/kg. The mice were fasted for 24 h at the end of the experiment. Sodium pentobarbital 150 mg/kg was injected intraperitoneally and the mice were executed by overdose anesthesia.

Hematoxylin and eosin staining
The tumor tissues were fixed in a 4% phosphate-buffered paraformaldehyde solution. The specimens were embedded in paraffin blocks and cut into 5-μm sections for hematoxylin and eosin (H&E) staining.

Immunohistochemistry
For immunohistochemistry, tissue sections were probed with several primary antibodies at 4 °C overnight: anti-mouse p Ki67 antibodies (1:50) (Servicebio, Wuhan, China), anti-VEGF rabbit antibody (1:200) (Servicebio, Wuhan, China), anti-CD4 rabbit antibody (1:500) (Servicebio, Wuhan, China), and anti-CD8 rabbit antibody (1:500) (Servicebio, Wuhan, China). This was followed by labeling with a peroxidase-conjugated secondary antibody (1:100) (Servicebio, Wuhan, China) at 37 °C for 1 h. Subsequently, a horseradish peroxidase–conjugated avidin/biotin complex system was used for visualization, with 3,3-diaminobenzidine solution used as the chromogen. Then, the sections were counterstained with hematoxylin and mounted on a cover slip. The optical density of the target protein was measured using Image-Pro Plus 6.0 software. The optical density was defined as the ratio of positive optical density to total pixels, representing the targeted protein quantity.

Hypoxia assays
Mice were injected intraperitoneally with 60 mg/kg pimonidazole HCl (Hypoxyprobe, Inc., Massachusetts, USA) dissolved in PBS 90 min before sacrifice to measure hypoxia within tumor tissues in the PBS, KLU, and QR-KLU groups. The tumor tissues were then collected, fixed with 4% paraformaldehyde for 2 h, and successively soaked in 20% (w/v) and 30% (w/v) PBS-buffered sucrose solution at 4 °C until the tumor tissues sank to the bottom of the tubes. The tissues were then embedded in the optimal cutting temperature (OCT) compound and cut into 5-μm sections. The sections were blocked in 10% (v/v) normal goat serum for 40 min at 37 °C, followed by incubation with mouse anti-pimonidazole antibody conjugated to DyLight 549 overnight at 4 °C. The nuclei were counterstained with 4′,6-diamidino-2-phenylindole dihydrochloride (DAPI), and the fluorescent images were obtained using a confocal laser-scanning microscope (Olympus, Japan).

Pericyte coverage evaluation
The tumor tissues were embedded in the OCT compound, and frozen sections were prepared for staining. The sections were then probed with APC-labeled rat anti-mouse CD31 antibody (1:100) (Servicebio, Wuhan, China), and mouse anti-mouse α-smooth muscle actin (α-SMA) antibody (1:500) (Servicebio, Wuhan, China) at 4 °C overnight, followed by labeling with Cy3-labeled goat anti-mouse secondary antibody (1:200) (Servicebio, Wuhan, China) at 37 °C for 1 h. The nuclei were counterstained with DAPI, and the fluorescent images were obtained using a confocal laser-scanning microscope (Olympus, Japan).

Flow cytometry testing
The tumors were excised and minced using surgical scissors, transferred to 50-mL tubes containing 10 mL of the Roswell Park Memorial Institute medium with 100 μL of collagenase IV (1 mg/mL, Sigma–Aldrich, MO, USA), and digested for 30 min at 37 °C. After termination of digestion, the cells were filtered through a filter membrane and resuspended in Hank's solution. Single-cell suspensions were then incubated with the following fluorescent-labeled antibodies at 4 °C for 40 min: FITC-labeled anti-mouse CD3 (Servicebio, Wuhan, China), PE-Cyanine7 dye-labeled anti-mouse CD4 (Servicebio, Wuhan, China), and APC-labeled anti-mouse CD8 (Servicebio, Wuhan, China) antibodies. The stained cells were then washed twice before being fixed with fluorescence-activated cell sorting buffer containing 4% paraformaldehyde and subjected to flow cytometry. The analysis was conducted using a Canto II flow cytometer (BD Biosciences, CA, USA), and the data were analyzed using the FlowJo software (Bd Biosciences, CA, USA).

Enzyme-linked immunosorbent assay
Blood was drawn from the eyes of mice before euthanasia, and the serum was subjected to enzyme-linked immunosorbent assay to evaluate the expression levels of tumor necrosis factor-α (TNF-α), interferon-γ (IFN-γ), interleukin-2 (IL-2), and IL-10 in the serum of each group.

Biological safety evaluation
Safety was evaluated by measuring liver and kidney function. The levels of alanine aminotransferase (ALT), aspartate aminotransferase (AST), total bilirubin (TBIL), blood urea nitrogen (BUN), and creatinine (CRE)

were assessed in the serum samples obtained at the end of the experiment. The assays were performed using commercially available kits (Abcam, Cambridge, USA) following the manufacturers' instructions.

The heart, lung, kidney, and spleen tissue samples were collected from the tumor-bearing mice after euthanasia and subjected to H&E staining to evaluate whether the drugs caused damage to systemic organs.

Statistical analysis

SPSS 25.0 (IBM, New York, USA) was used for data processing and statistical analysis, and GraphPad Prism 8.0 (GraphPad Prism, New York, USA) was used to generate relevant quantitative analysis graphics. All continuous variables were expressed as mean ± standard deviation. The Student t test was used to compare the variables between the 2 groups, and analysis of variance analysis was used to compare the variables among multiple groups. All significance tests were 2 tailed, and $P < 0.05$ indicated a statistically significant difference. Note: $***P < 0.001$, $**P < 0.01$, $*P < 0.05$; ns, no significant difference. The schematic illustrations were drawn using the Figdraw tool (www.figdraw.com).

Results

Effects of QR-KLU on normal red blood cells and HCC cell proliferation

Rabbit erythrocytes underwent hemolysis in the presence of 0.1% Triton X-100. However, the hemolysis rate remained stable even at high concentrations of peptides (QR: 160μM; KLU: 80μM; QR-KLU: 20μM) (Fig. 2A). These findings suggested that QR, KLU, and QR-KLU were safe and caused no erythrocyte lysis when applied to biological blood.

DOX, KLU, and QR-KLU substantially inhibited cell proliferation and exhibited dose dependency under both normoxic and hypoxic conditions (Fig. 2B). In Hepa1–6 cells, the half maximal inhibitory concentration (IC_{50}) value of DOX, KLU, and QR-KLU was 0.19μM, 38.9μM, and 15.0μM, respectively, under normoxic conditions,
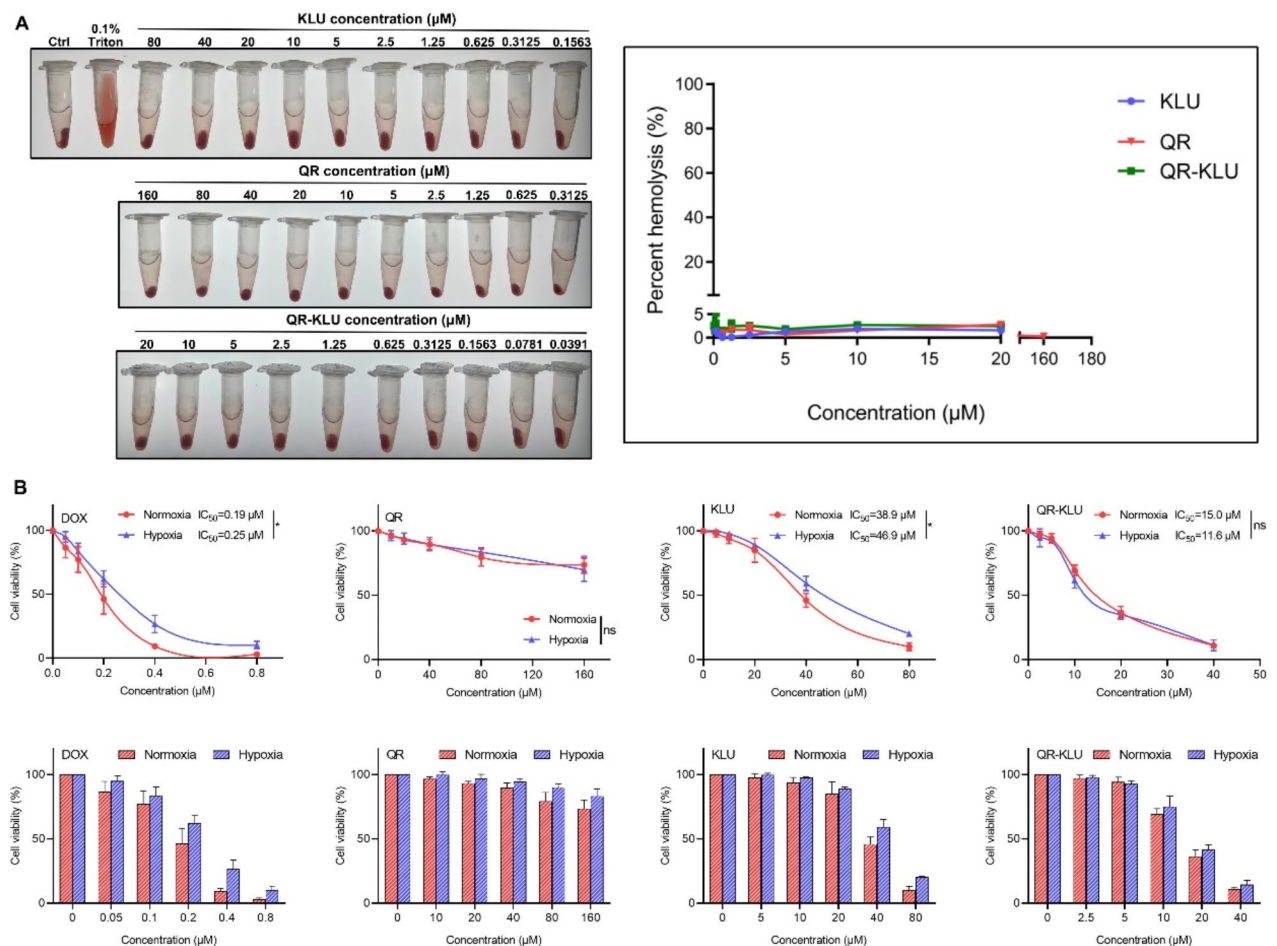

Fig. 2. Effects of QR-KLU on the toxicity to normal red blood cells and the proliferation activity of liver cancer cells ($n = 6$). (A) Representative hemolysis graphs of various concentrations of KLU, QR, and QR-KLU co-incubated with rabbit red blood cells. (B) CCK8 assay evaluating the effects of DOX, QR, KLU, and QR-KLU on the proliferation activity of Hepa1–6 cells under normoxic and hypoxic conditions. Hypoxic condition was created by adding 100 μM cobalt dichloride. *CCK8* cell counting kit-8, *DOX* doxorubicin, *QR-KLU* peptide (QR)–drug (KLU) conjugate.

and 0.25µM, 46.9µM, and 11.6µM, respectively, under hypoxic conditions. Thus, the IC_{50} values of DOX and KLU were substantially higher under hypoxic conditions than under normoxic conditions. In contrast, the IC_{50} value of QR-KLU exhibited no considerable difference between hypoxic and normoxic conditions.

Effects of QR-KLU on apoptosis and cell cycle of HCC cells

Compared with PBS, QR exhibited no increase in the proportion of apoptotic cells in Hepa1–6 cells cultured under normoxic and hypoxic conditions. However, treatment with KLU and QR-KLU substantially increased the proportion of apoptotic cells, with the QR-KLU group demonstrating a considerably higher proportion than the KLU group (Fig. 3A). Moreover, the proportion of S-phase cells increased considerably in Hepa1–6 cells treated with KLU and QR-KLU compared with those treated with PBS, with the QR-KLU group exhibiting a remarkable increase than the KLU group (Fig. 3B).
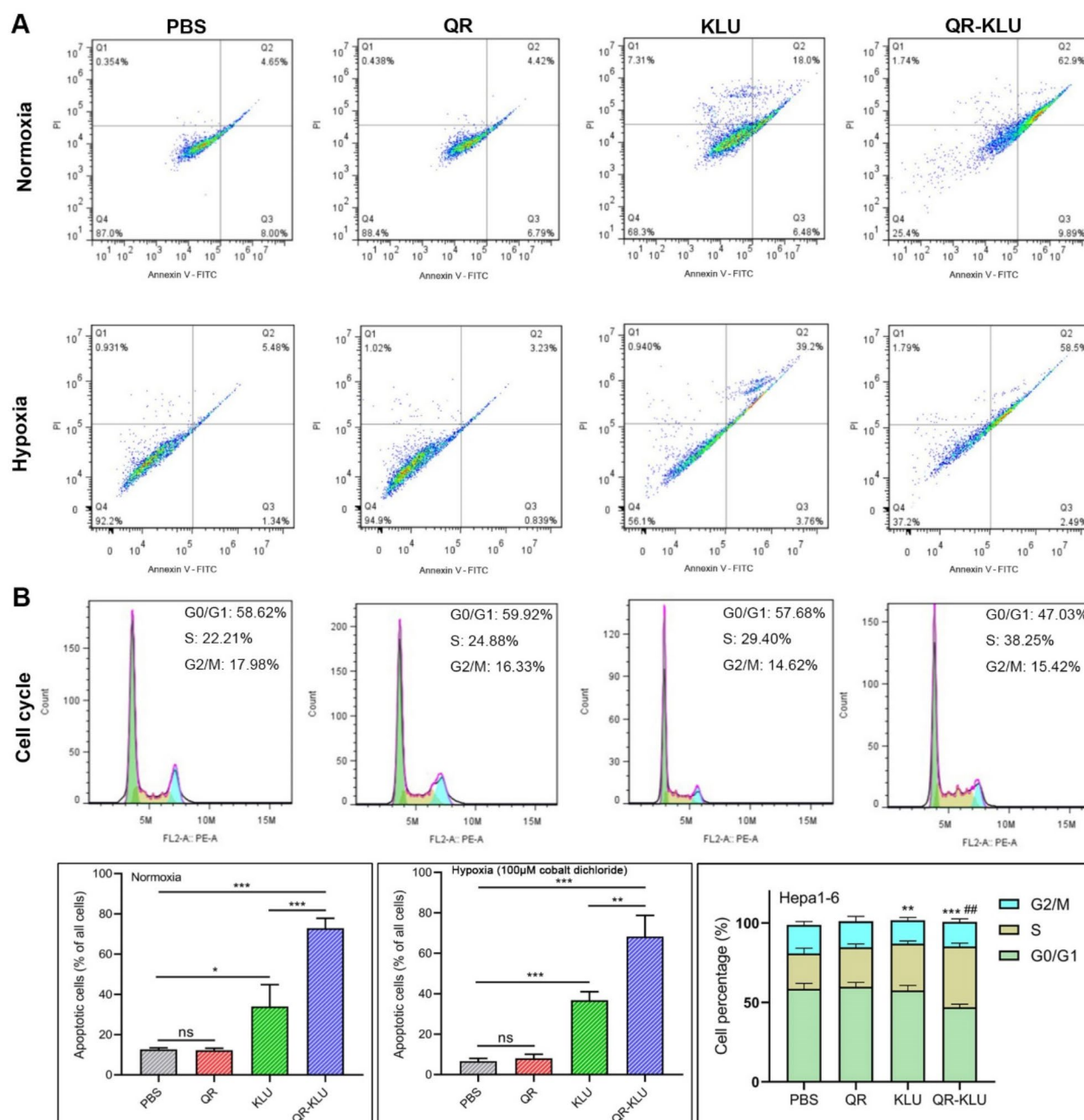

Fig. 3. Effects of QR-KLU on the apoptosis and cell cycle of liver cancer cells ($n = 6$). (**A**) Effects of QR, KLU, and QR-KLU on the apoptosis of Hepa1–6 cells under normoxic and hypoxic conditions. Hypoxic condition was created by adding 100 µM cobalt dichloride. (**B**) Effects of QR, KLU, and QR-KLU on the cell cycle of Hepa1–6 cells. *QR-KLU* peptide (QR)–drug (KLU) conjugate.

Effects of QR-KLU on cell migration and single-cell proliferation

No considerable difference in the proportion of scratch area was observed among the groups at 0 h under both normoxic and hypoxic conditions. At 48 h, the proportion of scratch area was considerably higher in the QR-KLU group than in the PBS and KLU groups (Fig. 4A and B). Additionally, the cell clone number was considerably lower in the KLU and QR-KLU groups than in the PBS group under both normoxic and hypoxic conditions. The QR-KLU group exhibited a considerably lower cell clone number than the KLU group (Fig. 4C). Moreover, the cell clone number of the Hepa1–6 cells increased under hypoxic conditions compared with normoxic conditions, and the advantage of QR-KLU over KLU was more evident under hypoxic conditions.

Effects of QR-KLU on HIF-1α and VEGF expression in HCC cells

Under hypoxic conditions, the relative expression levels of HIF-1α and VEGF were substantially higher in the Hepa1–6 cells of the PBS and QR-KLU groups than those under normoxic conditions (Fig. 4D). QR-KLU significantly downregulated VEGF expression even in normoxia. Moreover, the relative expression level of VEGF in the QR-KLU group was considerably lower than that in the PBS group under hypoxic conditions.
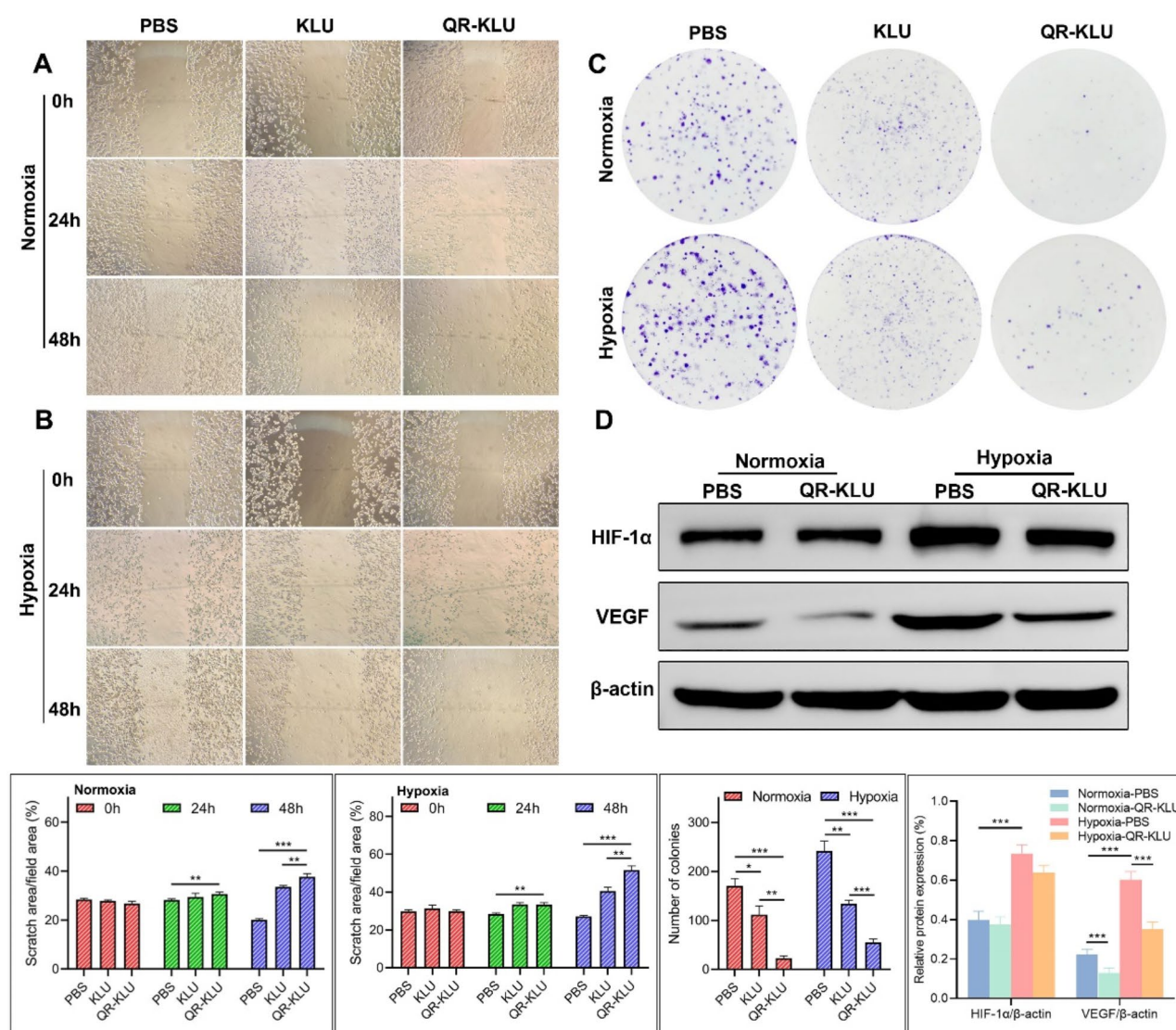

Fig. 4. Effects of QR-KLU on cell migration, single-cell proliferation, and the expression of HIF-1α and VEGF ($n = 6$). (**A**) Effects of KLU and QR-KLU on the migration ability of Hepa1–6 cells after 24 and 48 h of cultivation under normoxic conditions. Hypoxic condition was created by adding 100 μM cobalt dichloride. (**B**) Effects of KLU and QR-KLU on the migration ability of Hepa1–6 cells after 24 and 48 h of cultivation under hypoxic conditions. (**C**) Representative images of the plate clone of Hepa1–6 cells treated with KLU and QR-KLU under normoxic and hypoxic conditions. (**D**) Representative images of the expression of HIF-1α and VEGF in Hepa1–6 cells treated with PBS and QR-KLU under normoxic and hypoxic conditions. HIF-1α; *PBS* phosphate-buffered saline, *QR-KLU* peptide (QR)–drug (KLU) conjugate, *VEGF* vascular endothelial growth factor.

Effects of QR-KLU combined with anti-PD-1 antibody on subcutaneous tumor growth

A subcutaneous tumor model in mice was successfully established (Fig. 5A). Before the intervention, the average subcutaneous tumor volume of tumor-bearing mice in the PBS, KLU, QR-KLU, anti-PD-1, KLU + anti-PD-1, and QR-KLU + anti-PD-1 groups was 91.8 ± 9.3 mm^3, 95.3 ± 19.8 mm^3, 96.7 ± 13.2 mm^3, 85.6 ± 4.6 mm^3, 93.7 ± 13.7 mm^3, and 97.1 ± 13.7 mm^3, respectively. After the intervention, except for the QR-KLU + anti-PD-1 group, the tumor volume in all other groups gradually increased; the PBS group exhibited the fastest growth. The tumor volume growth rate was considerably lower in the QR-KLU + anti-PD-1 group than in the other groups. It even decreased compared with that before intervention on the 8th and 10th days (Fig. 5B). The average tumor volume in the PBS, KLU, QR-KLU, anti-PD-1, KLU + anti-PD-1, and QR-KLU + anti-PD-1 groups before euthanasia was 494.0 ± 90.4 mm^3, 223.3 ± 33.4 mm^3, 192.0 ± 53.0 mm^3, 309.1 ± 27.1 mm^3, 152.3 ± 37.0 mm^3, and 76.0 ± 10.5 mm^3, respectively. The average tumor volume was substantially lower in the QR-KLU + anti-PD-1 group than in other groups (Fig. 5C).

Effects of QR-KLU combined with anti-PD-1 antibody on the necrosis and proliferation of subcutaneous tumors

The average tumor necrosis rate in the PBS, KLU, QR-KLU, anti-PD-1, KLU + anti-PD-1, and QR-KLU + anti-PD-1 groups was $3.2\% \pm 0.9\%$, $37.1\% \pm 4.2\%$, $50.9\% \pm 3.7\%$, $5.0\% \pm 1.5\%$, $50.9\% \pm 3.9\%$, and $66.2\% \pm 3.0\%$, respectively (Fig. 6A). The necrosis rate was considerably higher in the QR-KLU group compared with the PBS and KLU groups, and the QR-KLU + anti-PD-1 group had substantially higher necrosis rates than the QR-KLU and anti-PD-1 groups. Additionally, Ki67 immunohistochemistry staining demonstrated that the average proportion of proliferating tumor cells was considerably lower in the QR-KLU group than in the PBS and KLU
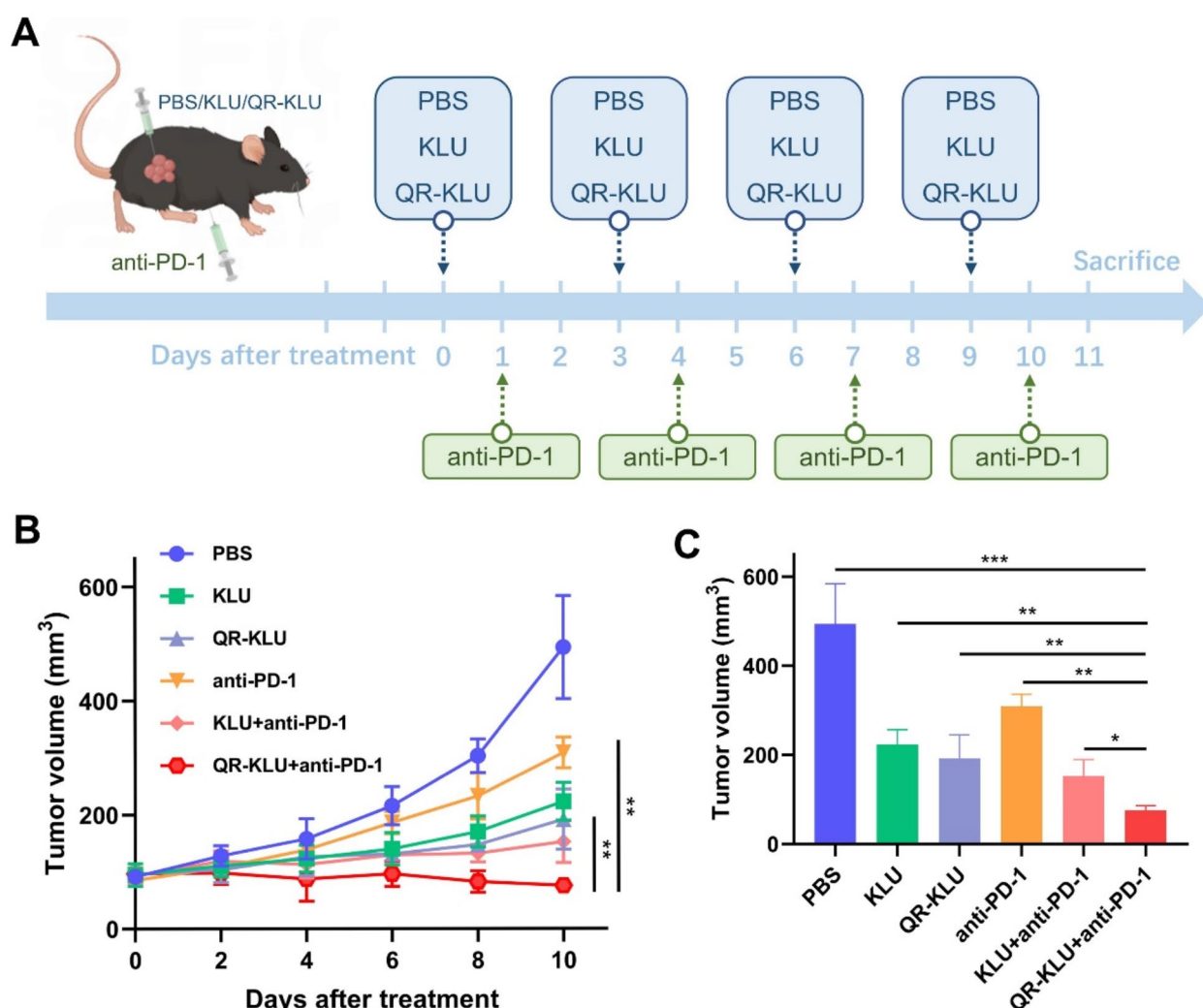

Fig. 5. Effects of QR-KLU combined with anti-PD-1 antibody on the growth of subcutaneous Hepa1–6 tumor in mice ($n = 6$). (**A**) Schematic diagram of the timing of intervention in Hepa1–6 tumor-bearing mice (drawn using Figdraw, export ID: YAPYSe1e88). (**B**) Tumor growth curve. (**C**) Bar chart of tumor volume at the last measurement. *PD-1* programmed cell death receptor-1, *QR-KLU* peptide (QR)–drug (KLU) conjugate.
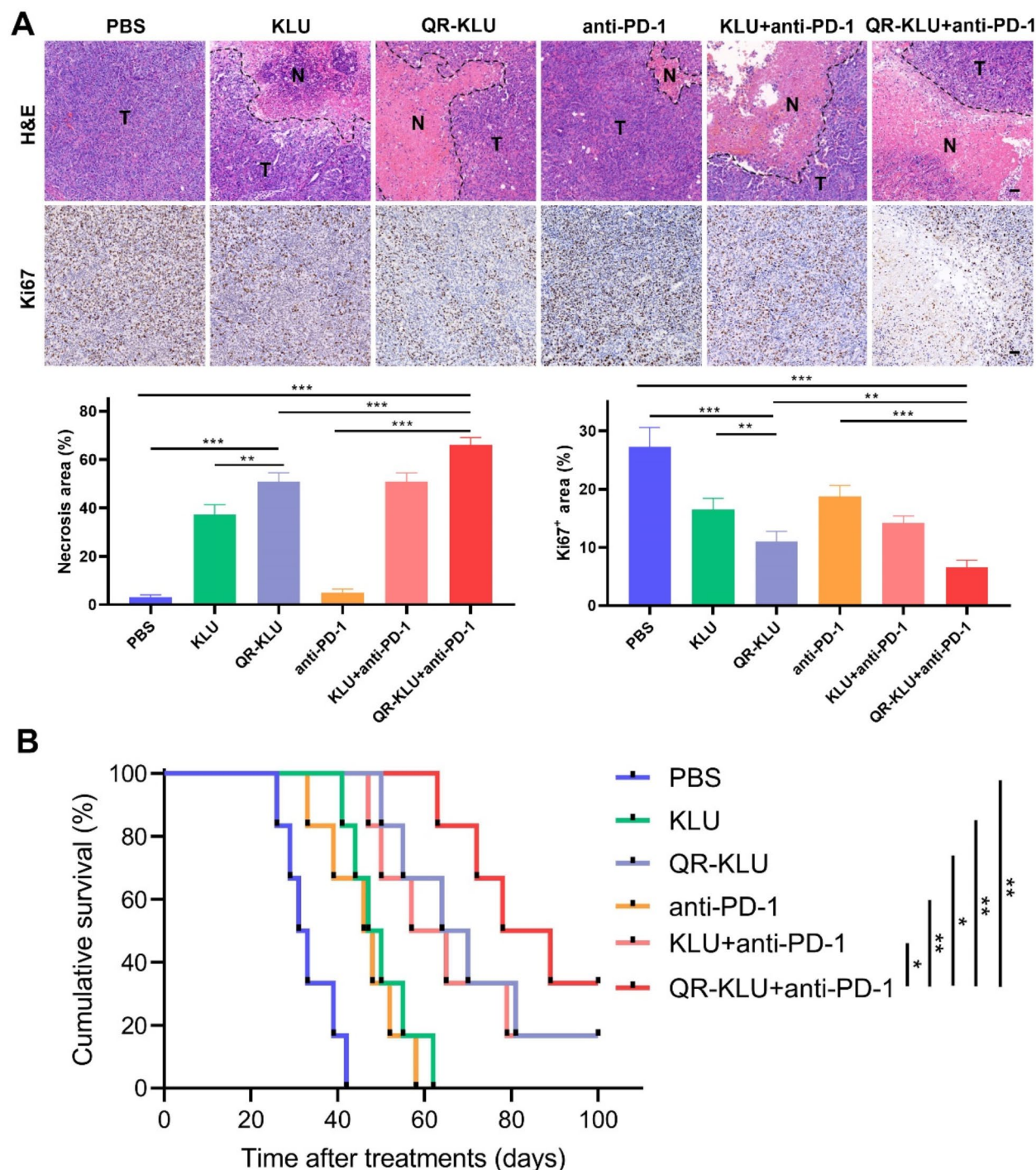
Fig. 6. Effects of QR-KLU combined with anti-PD-1 antibody on the necrosis and proliferation of subcutaneous Hepa1–6 liver tumors in mice ($n = 6$). (**A**) Necrosis and proliferation of subcutaneous Hepa1–6 liver tumors in each group of mice (N: tumor necrotic area; T: tumor nonnecrotic area). (**B**) Evaluation of the cumulative survival time of tumor-bearing mice in each group using Kaplan–Meier curve. *PD-1* programmed cell death receptor-1, *QR-KLU* peptide (QR)–drug (KLU) conjugate.

groups, and the proportion of proliferating cells was substantially lower in the QR-KLU + anti-PD-1 group than in the QR-KLU and anti-PD-1 groups (Fig. 6A).

Effects of QR-KLU combined with anti-PD-1 antibody on the survival of tumor-bearing mice

After the intervention, the survival time of each group of Hepa1–6 tumor-bearing mice was recorded until the 100th day. During this period, all mice in the PBS, KLU, and anti-PD-1 groups died, whereas 1 mouse each in the QR-KLU and KLU + anti-PD-1 groups and 2 mice in the QR-KLU + anti-PD-1 group remained tumor free. The

median survival time in the PBS, KLU, QR-KLU, anti-PD-1, KLU + anti-PD-1, and QR-KLU + anti-PD-1 groups was 32, 48.5, 67, 47, 61, and 83.5 days, respectively (Fig. 6B). Kaplan-Meier curve showed that the cumulative survival rate was substantially higher in the QR-KLU + anti-PD-1 group compared with the other groups.

Effects of QR-KLU on the tumor vascular normalization

The proportion of hypoxic regions in tumor tissues in the PBS, KLU, and QR-KLU groups was 14.2% ± 1.3%, 40.1% ± 2.2%, and 20.8% ± 2.0%, respectively. The proportion of hypoxic regions was remarkably higher in the KLU and QR-KLU groups than in the PBS group. In contrast, the proportion was considerably lower in the QR-KLU group than in the KLU group (Fig. 7A). The expression level of VEGF was substantially lower in the QR-KLU group than in the PBS and KLU groups. The level was considerably lower in the QR-KLU + anti-PD-1 group than in the anti-PD-1 group (Fig. 7B). The mean value of pericyte coverage of tumor blood vessels in the PBS, KLU, QR-KLU, anti-PD-1, and QR-KLU + anti-PD-1 groups was 22.3% ± 4.5%, 14.5% ± 3.5%, 66.8% ± 6.8%, 17.6% ± 3.1%, and 63.1% ± 6.1%, respectively. The pericyte coverage was remarkably higher in the QR-KLU group than in the PBS and KLU groups. The coverage was substantially higher in the QR-KLU + anti-PD-1 group than in the anti-PD-1 group (Fig. 7C). The intratumoral injection of KLU induced hypoxia in tumor tissues, leading to an increase in VEGF expression and further causing tumor vessel abnormalization. However, QR-KLU inhibited VEGF expression under hypoxic conditions by targeting VEGFR, promoting the normalization of tumor blood vessels.

Effects of QR-KLU combined with anti-PD-1 antibody on the number of intratumoral CD8 + T cells

The number of CD4$^+$ and CD8$^+$ T cells in tumor tissues was considerably higher in the KLU and QR-KLU groups than in the PBS group, and the number was substantially higher in the QR-KLU group than in the KLU group. In addition, the number of CD4$^+$ and CD8$^+$ T cells was substantially higher in the QR-KLU + anti-PD-1 group than in the QR-KLU and anti-PD-1 groups (Fig. 8A and B).

The expression levels of TNF-α and IFN-γ were remarkably higher in the QR-KLU group than in the PBS and KLU groups (Fig. 8C and D), and the levels were considerably higher in the QR-KLU + anti-PD-1 group than in the QR-KLU and anti-PD-1 groups. Meanwhile, the expression level of IL-2 was substantially higher in the QR-KLU + anti-PD-1 group compared with the other groups (Fig. 8E). In addition, the expression level of the immunosuppressive cytokine IL-10 was considerably lower in the QR-KLU + anti-PD-1 group compared with the other groups (Fig. 8F). Both KLU and QR-KLU could promote the infiltration of CD8$^+$ T cells into tumor tissues, and QR-KLU was superior to KLU. In addition, QR-KLU could synergistically promote the infiltration of CD8$^+$ T cells into tumor tissues with anti-PD-1 antibody and activate the expression of CD8$^+$ T cell activation factors, concurrently reducing the expression of immunosuppressive cytokines.

Biological safety

No substantial difference in the weight gain of mice (Fig. S1A) or the mean values of serum ALT, AST, TBIL, BUN, and CRE was observed among the groups (Fig. S1B–S1F). Using KLU, QR-KLU, and anti-PD-1 antibody alone or in combination resulted in no morphological changes or organic damage in the heart, lungs, liver, kidneys, and spleen of tumor-bearing mice (Figs S2 and S3).

Discussion

Immunotherapy with ICI alone or in combination with other drugs has been clinically effective in treating advanced HCC[30–32], as recommended by the guidelines[33,34]. The combination of PD-1 and PD-L1 can limit the activity of effector T cells, enabling tumors to evade immune surveillance[35]. Blocking their binding with PD-1 antibodies can promote the activation and infiltration of CD8$^+$ T cells into tumors and exert anti-tumor effects[36,37]. Nevertheless, the objective response rate of PD-1 antibodies in the treatment of advanced HCC is still less than 20%[30–32], and sustained clinical benefits are not achieved by most patients. Targeted anti-angiogenic drugs against VEGFR can promote tumor vascular normalization[38,39], relieving immune suppression caused by VEGF[40,41]. Therefore, researchers are now combining anti-PD-1 antibody with VEGFR-targeted drugs to treat advanced HCC, achieving more favorable results compared with monotherapy[42–45]. However, anti-PD-1 treatment failure rates have been higher for patients with high tumor burdens[46]. Therefore, reducing tumor burden remains crucial for treating advanced liver cancer with immunotherapy and anti-angiogenic therapy.

This study proposed a novel peptide-conjugated drug QR-KLU that remarkably reduced the tumor burden, inhibited liver cancer growth, and exerted cytotoxic effects on liver cancer cells and tumors. The QR peptide blocked VEGF signaling and promoted tumor vascular normalization. This study found that QR-KLU can increase pericyte coverage of tumor blood vessels, leading to the normalization of tumor vasculature. Vascular normalization can be influenced by various factors, including hypoxic conditions, drug delivery efficiency, and the presence of stromal cells, endothelial cells, or immune cells. In the future, we will conduct more in-depth research focusing on vascular normalization. QR-KLU combined with anti-PD-1 antibody targeted VEGFR to promote the infiltration of CD8$^+$ T cells into tumors, further reducing the tumor burden and synergistically enhancing the anti-liver cancer effect. Additionally, QR-KLU elevated the expression levels of TNF-α, IFN-γ, and IL-2, decreased the expression level of IL-10, and increased the number of CD8$^+$ T cells in tumors. When combined with anti-PD-1 antibody, QR-KLU further facilitated the infiltration of CD8$^+$ T cells into tumors and synergistically promoted the expression of CD8$^+$ T cell activation factors, simultaneously reducing the expression of immunosuppressive cytokines. We hypothesize that QR-KLU improves the immune microenvironment through immunogenic cell death or normalized vessel perfusion, which can reduce immune suppression and facilitate the transformation of a cold tumor into a hot tumor.
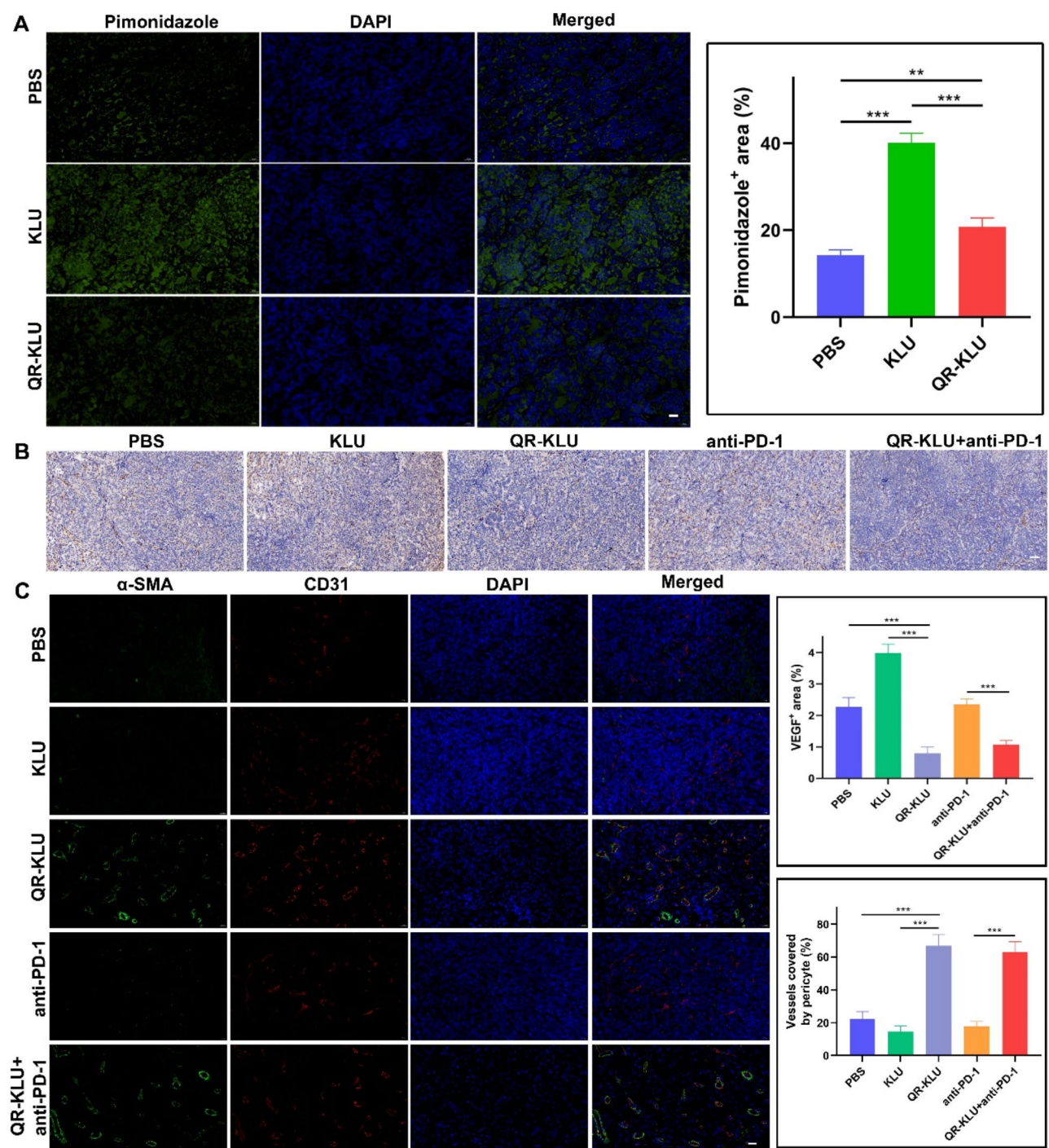
Fig. 7. Effects of QR-KLU on vascular normalization of subcutaneous Hepa1–6 liver tumors in mice ($n = 6$). (**A**) Representative immunofluorescence images of the hypoxia probe pimonidazole (scale bar = 20 μm; pimonidazole+: red; nucleus: blue). (**B**) Immunohistochemistry results of VEGF expression in subcutaneous Hepa1–6 liver tumors in mice treated with PBS, KLU, QR-KLU, anti-PD-1, and QR-KLU + anti-PD-1 (scale bar = 50 μm). (**C**) Representative immunofluorescence double-staining images of α-SMA and CD31 in subcutaneous Hepa1–6 liver tumors in mice treated with PBS, KLU, QR-KLU, anti-PD-1, and QR-KLU + anti-PD-1 (scale bar = 20 μm; α-SMA + pericytes: green; CD31 + endothelial cells: red; nucleus: blue). α-SMA, α-Smooth muscle actin; CD31; PBS, phosphate-buffered saline; P*PD-1* programmed cell death receptor-1, *QR-KLU* peptide (QR)–drug (KLU) conjugate, *VEGF* vascular endothelial growth factor.
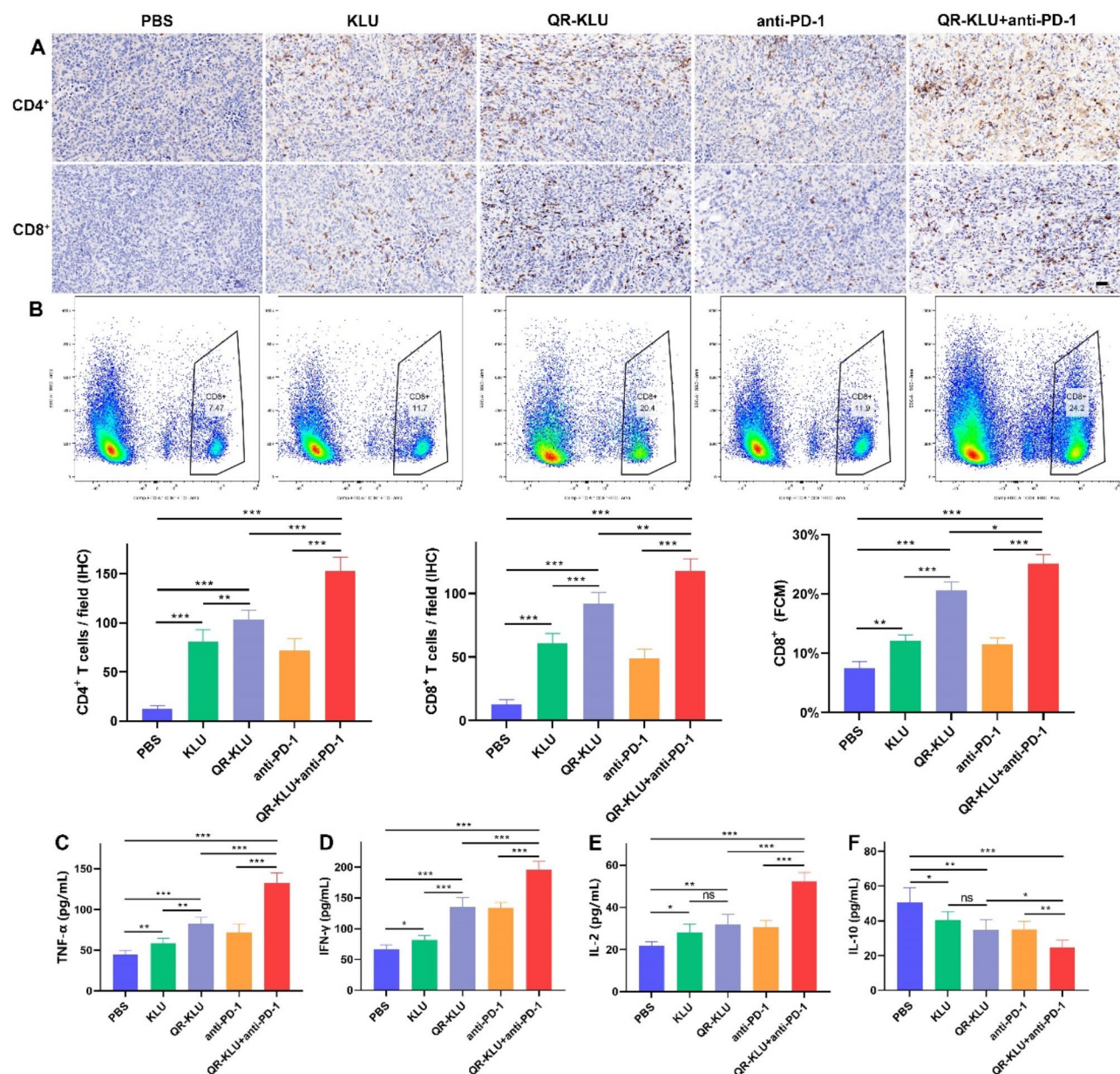
Fig. 8. Effects of QR-KLU combined with anti-PD-1 antibody on the immune cells and immune factors in subcutaneous Hepa1–6 liver tumors in mice ($n = 6$). (**A**) Representative immunohistochemistry staining images of CD4+ and CD8+ cells (scale bar $= 20\ \mu m$). (**B**) Determination of the number of CD8+ cells using flow cytometry. (**C**) Bar graph demonstrating TNF-α expression levels. (**D**) Bar graph demonstrating IFN-γ expression levels. (**E**) Bar graph demonstrating IL-2 expression levels. (**F**) Bar graph demonstrating IL-10 expression levels. *α-SMA* α-smooth muscle actin, *CD; IFN-γ* interferon-γ, *PD-1* programmed cell death receptor-1, *QR-KLU* peptide (QR)–drug (KLU) conjugate, *TNF-α* tumor necrosis factor-α, *VEGF* vascular endothelial growth factor.

Chen et al. reduced the tumor burden in a lung tumor model by combining radiotherapy with ICI and anti-VEGF therapy to promote the local accumulation of CD8+ T cells and reduce MDSC, leading to tumor growth inhibition and improved survival rates in tumor-bearing mice[47]. Bao et al. treated H22 liver cancer subcutaneous tumor models in mice using a vascular disruptor and VEGFR inhibitor combined with PD-1 antibodies[48]. The vascular disruptor reduced the tumor burden and the VEGFR inhibitor promoted vascular normalization, both of which increased the number of CD8+ T cells in tumors and improved the efficacy of PD-1 antibodies. Moreover, reducing the tumor burden and blocking the VEGF pathway could enhance the efficacy of immunotherapy regardless of the tumor type. Therefore, QR-KLU is a promising agent for ICI treatment of advanced liver cancer and can be used in combination with PD-1 antibodies to treat advanced HCC.

This study had several limitations. First, it failed to account for the impact of tumor heterogeneity on the results and neglected to assess the drug's sensitivity to various tumor parts. Moreover, the study failed to perform dynamic evaluations of the therapeutic effect through functional imaging and other methods.

Conclusions

In this study, a novel peptide-conjugated drug QR-KLU was designed and synthesized, which could effectively inhibit the growth of liver cancer cells and high expression of VEGF under both normoxic and hypoxic conditions. QR-KLU combined with anti-PD-1 antibody synergistically inhibited liver tumor growth, promoted tumor necrosis and vascular normalization, and increased the infiltration of CD8$^+$ T cells into tumors. These findings suggested that QR-KLU had strong potential as a liver cancer treatment drug with promising clinical applications.

Data availability

Data described in the manuscript will be made available upon request pending application and approval from the corresponding author.

References

1. Wang, Y. & Deng, B. Hepatocellular carcinoma: molecular mechanism, targeted therapy, and biomarkers. *Cancer Metastasis Rev.* https://doi.org/10.1007/s10555-023-10084-4 (2023).
2. Ioannou, G. N. HCC surveillance after SVR in patients with F3/F4 fibrosis. *J. Hepatol.* **74**, 458–465. https://doi.org/10.1016/j.jhep.2020.10.016 (2021).
3. Rumgay, H. et al. Global burden of primary liver cancer in 2020 and predictions to 2040. *J. Hepatol.* **77**, 1598–1606. https://doi.org/10.1016/j.jhep.2022.08.021 (2022).
4. Sangro, B. et al. Advances in immunotherapy for hepatocellular carcinoma. *Nat. Rev. Gastroenterol. Hepatol.* **18**, 525–543. https://doi.org/10.1038/s41575-021-00438-0 (2021).
5. Greten, T. F. et al. Targeted and Immune-based therapies for Hepatocellular Carcinoma. *Gastroenterology*. **156**, 510–524. https://doi.org/10.1053/j.gastro.2018.09.051 (2019).
6. Pham, L. et al. The functional roles of Immune cells in primary Liver Cancer. *Am. J. Pathol.* **192**, 826–836. https://doi.org/10.1016/j.ajpath.2022.02.004 (2022).
7. Chen, M. et al. HIF-2α-targeted interventional chemoembolization multifunctional microspheres for effective elimination of hepatocellular carcinoma. *Biomaterials*. **284**, 121512. https://doi.org/10.1016/j.biomaterials.2022.121512 (2022).
8. Chen, L. et al. ARL13B promotes angiogenesis and glioma growth by activating VEGFA-VEGFR2 signaling. *Neuro Oncol.* **25**, 871–885. https://doi.org/10.1093/neuonc/noac245 (2023).
9. Tang, W. et al. The mechanisms of sorafenib resistance in hepatocellular carcinoma: theoretical basis and therapeutic aspects. *Signal Transduct. Target. Ther.* **5**, 87. https://doi.org/10.1038/s41392-020-0187-x (2020).
10. Hu, Z. et al. Exosome-derived circCCAR1 promotes CD8 + T-cell dysfunction and anti-PD1 resistance in hepatocellular carcinoma. *Mol. Cancer*. **22**, 55. https://doi.org/10.1186/s12943-023-01759-1 (2023).
11. Saez-Ibanez, A. R., Upadhaya, S. & Campbell, J. Immuno-Oncology clinical trials take a turn beyond PD1/PDL1 inhibitors. *Nat. Rev. Drug Discov.* **22**, 442–443. https://doi.org/10.1038/d41573-023-00066-0 (2023).
12. Gabrilovich, D. I. et al. Production of vascular endothelial growth factor by human tumors inhibits the functional maturation of dendritic cells. *Nat. Med.* **2**, 1096–1103 (1996).
13. Oyama, T. et al. Vascular endothelial growth factor affects dendritic cell maturation through the inhibition of nuclear factor-kappa B activation in hemopoietic progenitor cells. *J. Immunol.* **160**, 1224–1232 (1998).
14. Voron, T. et al. Control of the immune response by pro-angiogenic factors. *Front. Oncol.* **4**, 70. https://doi.org/10.3389/fonc.2014.00070 (2014).
15. Tyagi, A. et al. CancerPPD: a database of anticancer peptides and proteins. *Nucleic Acids Res.* **43**, D837-D843. https://doi.org/10.1093/nar/gku892 (2015).
16. Li, Y. et al. Lycorine transfersomes modified with cell-penetrating peptides for topical treatment of cutaneous squamous cell carcinoma. *J. Nanobiotechnol.* **21**, 139. https://doi.org/10.1186/s12951-023-01877-4 (2023).
17. Qiu, J. et al. Microfluidic formulation of anticancer peptide loaded ZIF-8 nanoparticles for the treatment of breast cancer. *J. Colloid Interface Sci.* **642**, 810–819. https://doi.org/10.1016/j.jcis.2023.03.172 (2023).
18. Yuan, Q. et al. Prediction of anticancer peptides based on an ensemble model of deep learning and machine learning using ordinal positional encoding. *Brief. Bioinform.* **24** https://doi.org/10.1093/bib/bbac630 (2023).
19. Chiangjong, W., Chutipongtanate, S. & Hongeng, S. Anticancer peptide: physicochemical property, functional aspect and trend in clinical application (review). *Int. J. Oncol.* **57**, 678–696. https://doi.org/10.3892/ijo.2020.5099 (2020).
20. Ghaly, G. et al. Anti-cancer peptides: Status and Future prospects. *Molecules*. https://doi.org/10.3390/molecules28031148 (2023).
21. Norouzi, P., Mirmohammadi, M., Houshdar, M. H. & Tehrani Anticancer peptides mechanisms, simple and complex. *Chem. Biol. Interact.* **368**, 110194. https://doi.org/10.1016/j.cbi.2022.110194 (2022).
22. Jia, H. et al. Peptides encoded by exon 6 of VEGF inhibit endothelial cell biological responses and angiogenesis induced by VEGF. *Biochem. Biophys. Res. Commun.* **283**, 164–173 (2001).
23. Hu, K. et al. PET imaging of VEGFR with a Novel 64Cu-Labeled peptide. *ACS Omega*. **5**, 8508–8514. https://doi.org/10.1021/acsomega.9b03953 (2020).
24. Qin, Z. et al. Imaging targeted at tumor with (188)re-labeled VEGF(189) exon 6-encoded peptide and effects of the transfecting truncated KDR gene in tumor-bearing nude mice. *Nucl. Med. Biol.* **36**, 535–543. https://doi.org/10.1016/j.nucmedbio.2009.02.001 (2009).
25. Zhao, H. et al. The development of activatable lytic peptides for targeting triple negative breast cancer. *Cell. Death Discov.* **3**, 17037. https://doi.org/10.1038/cddiscovery.2017.37 (2017).
26. Wang, D. et al. A VEGFR targeting peptide-drug conjugate (PDC) suppresses tumor angiogenesis in a TACE model for hepatocellular carcinoma therapy. *Cell. Death Discov.* **8**, 411. https://doi.org/10.1038/s41420-022-01198-9 (2022).
27. Liang, L. et al. The reversion of DNA methylation-induced miRNA silence via biomimetic nanoparticles-mediated gene delivery for efficient lung adenocarcinoma therapy. *Mol. Cancer*. **21**, 186. https://doi.org/10.1186/s12943-022-01651-4 (2022).
28. Liang, C. C., Park, A. Y. & Guan, J. L. In vitro scratch assay: a convenient and inexpensive method for analysis of cell migration in vitro. *Nat. Protoc.* **2**, 329–333 (2007).

29. Li, L. et al. Radiofrequency-responsive dual-valent gold nanoclusters for enhancing synergistic therapy of tumor ablation and artery embolization. *Nano Today*. **35**, 100934. https://doi.org/10.1016/j.nantod.2020.100934 (2020).
30. El-Khoueiry, A. B. et al. Nivolumab in patients with advanced hepatocellular carcinoma (CheckMate 040): an open-label, non-comparative, phase 1/2 dose escalation and expansion trial. *Lancet (London England)*. **389**, 2492–2502. https://doi.org/10.1016/S0140-6736(17)31046-2 (2017).
31. Zhu, A. X. et al. Pembrolizumab in patients with advanced hepatocellular carcinoma previously treated with sorafenib (KEYNOTE-224): a non-randomised, open-label phase 2 trial. *Lancet Oncol.* **19**, 940–952. https://doi.org/10.1016/S1470-2045(18)30351-6 (2018).
32. Verset, G. et al. Pembrolizumab Monotherapy for previously untreated Advanced Hepatocellular Carcinoma: data from the Open-Label, phase II KEYNOTE-224 trial. *Clin. Cancer Res.* **28**, 2547–2554. https://doi.org/10.1158/1078-0432.CCR-21-3807 (2022).
33. Reig, M. et al. BCLC strategy for prognosis prediction and treatment recommendation: the 2022 update. *J. Hepatol.* **76**, 681–693. https://doi.org/10.1016/j.jhep.2021.11.018 (2022).
34. Brahmer, J. R. et al. Society for Immunotherapy of Cancer (SITC) clinical practice guideline on immune checkpoint inhibitor-related adverse events. *J. Immunother. Cancer.* **9**. https://doi.org/10.1136/jitc-2021-002435 (2021).
35. Sharpe, A. H. & Pauken, K. E. The diverse functions of the PD1 inhibitory pathway. *Nat. Rev. Immunol.* **18**, 153–167. https://doi.org/10.1038/nri.2017.108 (2018).
36. Baumeister, S. H. et al. Coinhibitory pathways in Immunotherapy for Cancer. *Annu. Rev. Immunol.* **34**, 539–573. https://doi.org/10.1146/annurev-immunol-032414-112049 (2016).
37. Serratì, S. et al. Circulating extracellular vesicles expressing PD1 and PD-L1 predict response and mediate resistance to checkpoint inhibitors immunotherapy in metastatic melanoma. *Mol. Cancer.* **21**, 20. https://doi.org/10.1186/s12943-021-01490-9 (2022).
38. Cao, Y., Langer, R. & Ferrara, N. Targeting angiogenesis in oncology, ophthalmology and beyond. *Nat. Rev. Drug Discov.* **22**, 476–495. https://doi.org/10.1038/s41573-023-00671-z (2023).
39. Huang, C. et al. BICC1 drives pancreatic cancer progression by inducing VEGF-independent angiogenesis. *Signal. Transduct. Target. Ther.* **8**, 271. https://doi.org/10.1038/s41392-023-01478-5 (2023).
40. Xiong, Z. et al. Targeting PPAR-gamma counteracts tumour adaptation to immune-checkpoint blockade in hepatocellular carcinoma. *Gut.* https://doi.org/10.1136/gutjnl-2022-328364 (2023).
41. Wang, M. et al. Therapeutic blocking of VEGF binding to neuropilin-2 diminishes PD-L1 expression to activate antitumor immunity in prostate cancer. *Sci. Transl Med.* **15**, eade5855. https://doi.org/10.1126/scitranslmed.ade5855 (2023).
42. Kikuchi, H. et al. Increased CD8 + T-cell infiltration and efficacy for multikinase inhibitors after PD-1 blockade in Hepatocellular Carcinoma. *J. Natl. Cancer Inst.* **114**, 1301–1305. https://doi.org/10.1093/jnci/djac051 (2022).
43. Esteban-Fabró, R. et al. Cabozantinib enhances Anti-PD1 activity and elicits a neutrophil-based Immune Response in Hepatocellular Carcinoma. *Clin. Cancer Res.* **28**, 2449–2460. https://doi.org/10.1158/1078-0432.CCR-21-2517 (2022).
44. Fulgenzi, C. A. M. et al. Comparative efficacy of novel combination strategies for unresectable hepatocellular carcinoma: a network metanalysis of phase III trials. *Eur. J. Cancer.* **174**, 57–67. https://doi.org/10.1016/j.ejca.2022.06.058 (2022).
45. Sukowati, C., Cabral, L. K. D. & Tiribelli, C. Immune checkpoint and angiogenic inhibitors for the treatment of hepatocellular carcinoma: it takes two to tangle. *Ann. Hepatol.* **27**, 100740. https://doi.org/10.1016/j.aohep.2022.100740 (2022).
46. Huang, A. C. et al. T-cell invigoration to tumour burden ratio associated with anti-PD-1 response. *Nature.* **545**, 60–65. https://doi.org/10.1038/nature22079 (2017).
47. Chen, J. L. Y. et al. Evaluation of antitumor immunity by a combination treatment of high-dose irradiation, anti-PDL1, and anti-angiogenic therapy in murine lung tumors. *Cancer Immunol. Immunother.* **70**, 391–404. https://doi.org/10.1007/s00262-020-02690-w (2021).
48. Bao, X. et al. Enhanced anti-PD-1 therapy in hepatocellular carcinoma by tumor vascular disruption and normalization dependent on combretastatin A4 nanoparticles and DC101. *Theranostics.* **11**, 5955–5969. https://doi.org/10.7150/thno.58164 (2021).

Acknowledgements

Author contributions

Jiacheng Liu: Conceptualization; Methodology; Writing – original draft. Yaowei Bai: Conceptualization; Methodology. Xiaoming Liu: Conceptualization; Methodology. Binqian Zhou, Peng Sun, and Yingliang Wang: Data curation. Shuguang Ju, Chen Zhou, Chaoyang Wang, Wei Yao, Huihui Yang and Xin Jiang: Methodology. Lian Yang, Dongyuan Wang, and Chuansheng Zheng: Conceptualization, Writing – review & editing.

Declarations

Competing interests

The authors declare no competing interests.

Ethics approval

The study protocol conformed to the guidelines of the ARRIVE and was approved by the Ethics Committee of Tongji Medical College, Huazhong University of Science and Technology.

Additional information

Supplementary Information The online version contains supplementary material available at https://doi.org/10.1038/s41598-024-72907-w.

Correspondence and requests for materials should be addressed to L.Y., D.W. or C.Z.

Reprints and permissions information is available at www.nature.com/reprints.

Publisher's note Springer Nature remains neutral with regard to jurisdictional claims in published maps and institutional affiliations.